Chemical Science

Accepted Manuscript

This article can be cited before page numbers have been issued, to do this please use: W. Lin, S. Niu, S. Wu and C. Fang, *Chem. Sci.*, 2026, DOI: 10.1039/D6SC03942A.

ROYAL SOCIETY OF CHEMISTRY

rsc.li/chemical-science

View Article Online
DOI: 10.1039/D6SC03942A

Engineering Asymmetric Solvation Structures for Synergistically Boosted Quasi-Solid Thermocells

Wentao Lin[a], Shuo Niu[a], Shukai Wu[a], Chao Fang[a,*]

[a] Sustainable Energy and Environment Thrust, The Hong Kong University of Science and Technology (Guangzhou), Guangzhou, 511400, Guangdong, China

*Corresponding author:
chaofang@hkust-gz.edu.cn

View Article Online
DOI: 10.1039/D6SC03942A

ABSTRACT

Quasi solid-state thermocells (QTECs) based on the thermogalvanic effect offer a promising route for directly converting abundant low-grade heat into electricity. Introducing a single solvent into hydrogel electrolytes, a common strategy to enhance thermopower, often yields marginal solvation entropy difference between redox ions and provides limited gains in ion transport. To break this longstanding trade-off, we present a simple yet highly effective co-solvents strategy that employes trimethyl phosphate and ethylene glycol to construct hybrid hydrogel electrolytes. This approach synergistically enlarges solvation entropy differences of redox ions, amplifies concentration gradient across the thermocell, and enhances redox ion transport through hydrogel network. The resulting hydrogel electrolyte achieves superior thermoelectrochemical performance and demonstrates efficient harvesting of low-grade heat even at sub-zero temperatures. Advanced characterization techniques, integrated with molecular simulations, elucidate that the enhanced thermoelectrochemical performance originates from co-solvent engineered asymmetric solvation structures. This work demonstrates targeted, additive-free modulation of the solvation environment in thermogalvanic hydrogels as a practical strategy for significantly enhancing thermoelectrochemical performance.

View Article Online
DOI: 10.1039/D6SC03942A

I. INTRODUCTION

The pursuit of effective and sustainable waste heat utilization techniques is crucial for global energy conservation and achieving carbon neutrality goals.[1-5] At present, approximately 60% of the world's energy is ultimately wasted as heat, most of which is low-grade heat (< 100 °C).[6, 7] Thermocells (TECs), which operate based on the thermogalvanic effect, have attracted growing attention due to their promising capacity for harvesting waste low-grade heat.[8-12] A typical TEC consists of two electrodes separated by an electrolyte containing redox couple ions. When a temperature gradient (ΔT) is applied between the electrodes, an electric potential difference develops through temperature-driven redox reactions, thus allowing nonintermittent heat-to-electricity conversion. Recently, quasi solid-state TECs (QTECs) based on hydrogel electrolytes (thermogalvanic hydrogels, THs) have attracted considerable interest as a practical and scalable platform to harvesting low-grade thermal energy, particularly for self-powered wearable electronics.[13, 14] These systems are recognized for their considerable thermopower (known as Seebeck coefficient, S_e), which often exceeds 1 mV K^{-1}, alongside advantages such as low costs.[15-19]

The solvation structure of redox ions is a critical factor governing the thermoelectrochemical performance of THs, as it directly determines the entropy change (ΔS_{rc}) of the redox reaction.[12, 17, 20-22] In the case of a widely used redox couple, $Fe(CN)_6^{4-/3-}$,[23-27] the high-valence ion experiences a stronger charge-dipole interactions with surrounding solvent molecules, which leads to a more ordered solvation shell than that of $Fe(CN)_6^{3-}$. Such difference in local solvation structure generates disparity in the temperature-dependent response of the solvation free energy between two redox ions, essentially solvation entropy. This term contributes to the overall entropy change of redox reaction, as captured in the thermodynamic expression of S_e:[28]

$$S_e = \frac{\Delta E}{\Delta T n F} = \frac{\Delta S_{rc}}{nF} = \frac{\Delta S_{solv} + \Delta S_{conc}}{nF} \qquad (1)$$

where ΔE is the potential difference developed across ΔT, n is the number of electrons

View Article Online
DOI: 10.1039/D6SC03942A

transferred, and F is the Faraday's constant. This expression decouples ΔS_{rc} into contributions from ion solvation (ΔS_{solv}) and concentration (ΔS_{conc}). In particular, ΔS_{solv} arises from the difference in the ratio of the redox ions' activity coefficients between the two electrodes (equivalently, solvation entropy difference). On the other hand, ΔS_{conc} scales with the difference in the ratio of the redox ions' concentrations between the electrodes. Importantly, the ΔS_{conc} term itself is affected by ion solvation, as solvation dictates the solubility of redox ions. [18, 29-31] Therefore, even minor changes in the ordering and dynamics of the local ion solvation environment can significantly influence the thermoelectrochemical performance.[17, 32-34]

A high S_e is desirable for practical applications, particularly for powering IoT sensors or wearable devices, where efficient utilization of low-grade heat under small ΔT is indispensable for sustainable operation. Recent research has demonstrated that S_e can be effectively enhanced by introducing organic solvents.[29, 31, 35] For example, a study on ethylene glycol (EG)/polyacrylamide (PAAm)-based TH demonstrated through spectral characterization that EG modifies the solvation structures and solubility of $Fe(CN)_6^{4-/3-}$ ions.[31] Consequently, S_e was boosted from 1.30 to 2.04 mV K^{-1} with this alteration. In another study with bacterial cellulose-based TH, the introduction of propylene glycol induced selective reconstruction of the $Fe(CN)_6^{4-}$ solvation shell, which contributed to a high S_e of 2.30 mV K^{-1}.[29] Despite these improvements, a fundamental challenge persists for practical deployment of single-solvent THs. The inverse relationship between key electrolyte properties, such as S_e and ionic conductivity σ, severely compromises the output power density, thereby limiting the energy-harvesting capability of QTECs.

Herein, we develop a co-solvents engineering strategy employing trimethyl phosphate (TMP) and EG within a polyacrylamide (PAAm) hydrogel to construct asymmetric solvation structures and enable efficient ion transport. Although EG is known to modulate solvation structures, its capacity to compete with water molecules in the primary solvation shell of $Fe(CN)_6^{4-/3-}$ is mitigated by the resemblance of hydroxyl groups to water. To

View Article Online
DOI: 10.1039/D6SC03942A

address this constraint, we introduced TMP, an unexplored solvent molecule in thermocells that features highly polar phosphate ester group, to more effectively reconstruct the solvation structures of $Fe(CN)_6^{4-/3-}$. The combination of TMP and EG was found to synergistically enlarge the solvation entropy difference and amplify concentration gradients of the redox ions as captured by Eq. 1. This effect, together with enhanced ion-polymer interaction and salt dissociation, delivers exceptional thermoelectrochemical performance in the co-solvents hydrogel electrolytes that persists even at sub-zero temperatures. Our work provides a practical strategy and new insights for the design of high-performance QTECs via the rational, additive-free manipulation of the solvation environment.

II. RESULTS

Characteristics of Co-solvents Hydrogel Electrolyte

The design strategy for enhancing the thermoelectrochemical performance of hydrogel electrolyte is illustrated in **Figure 1**. A co-solvents (EG/TMP) hydrogel electrolyte (**Figure 1a**) was fabricated via a standard two-step procedure as shown in **Figure S1**. Initially, acrylamide, initiators, and crosslinkers were dissolved in ultrapure water and stirred to form a homogeneous solution. The solution was subsequently injected into a glass plat mold and heated to form a pure PAAm hydrogel. Next, EG solvent, TMP solvent, and $K_3Fe(CN)_6$-$K_4Fe(CN)_6$ salt were incorporated into the PAAm hydrogel via solution exchange. This yields a hydrogel electrolyte containing both aqueous and organic solvents. To investigate the relationship between intermolecular interactions and thermoelectrochemical performance, a series of parallel electrolytes were prepared with varying EG-to-TMP ratios. For clarity, the hydrogel electrolyte systems were designated as "Hybrid-E_xT_y" (short for "Hybrid-$(EG)_x(TMP)_y$"), where x and y respectively denote the volume percentages of EG and TMP in the solution phase.

The continuous operation of the Hybrid-E_xT_y-based QTEC is sustained by the thermal voltage generated between the cold and hot sides under ΔT. The magnitude of this voltage,

View Article Online
DOI: 10.1039/D6SC03942A

characterized by S_e, is determined by the solvation entropy difference between two redox ions and their concentration gradients between the hot and cold electrodes, as illustrated by Eq. 1. The Hybrid-E_xT_y system demonstrates excellent thermoelectrochemical performance as compared to both pure PAAm electrolyte and single-solvent hydrogel electrolytes. The enhancement in solvation entropy difference mainly originates from co-solvents (EG and TMP) induced restructuring of the solvation environment of redox ions. Due to the preferential interaction between $Fe(CN)_6^{4-}$ and co-solvents, greater number of solvent molecules are recruited into the solvation shell as compared to $Fe(CN)_6^{3-}$. This results in more asymmetric solvation structures to effectively enlarge their solvation entropy difference (**Figure 1b**). Meanwhile, the accessibility of coordination sites along the PAAm backbone to $Fe(CN)_6^{4-/3-}$ is modulated by the co-solvents. The induced differential polymer-ion interactions further amplify the solvation entropy difference between redox ions.

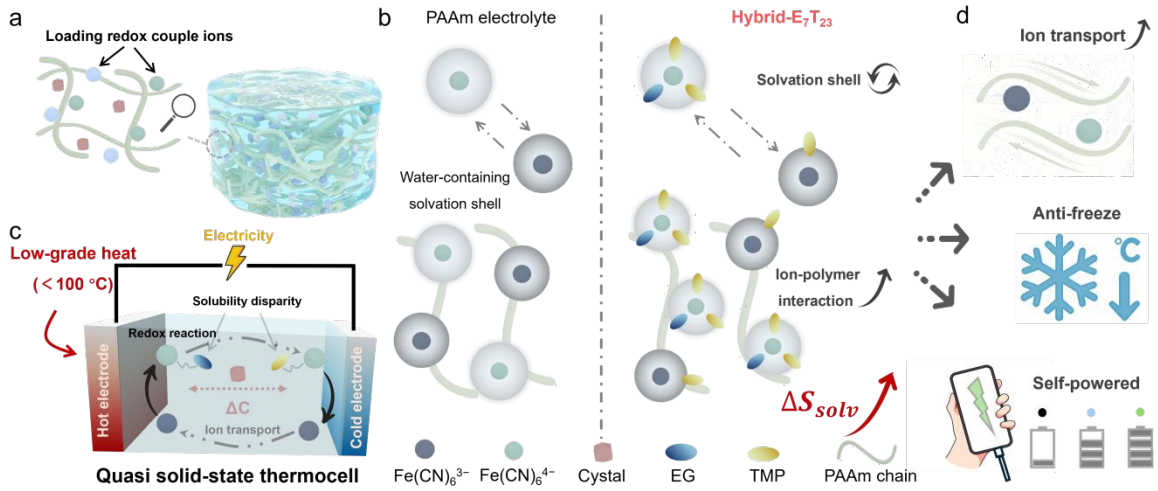

Figure 1. Design strategy of co-solvents hydrogel electrolyte. (a) Schematic of the Hybrid-E_xT_y assembly. **(b)** Comparison of ion solvation structure and ion-polymer interactions between the PAAm and Hybrid-E_7T_{23} electrolytes. **(c)** Co-solvents induced crystallization of $Fe(CN)_6^{4-}$ and its role in enhancing the thermogalvanic effect. **(d)** Illustration of enhanced ion transport and anti-freeze properties of Hybrid-E_7T_{23}, along with its potential applications.

View Article Online
DOI: 10.1039/D6SC03942A

The restructuring of solvation environment also leads to a marked alteration in the thermodynamic solubility of redox ions, as depicted in **Figure 1c**. $Fe(CN)_6^{4-}$ exhibits significantly lower solubility relative to $Fe(CN)_6^{3-}$, primarily due to the different ion-solvent interactions that tends to stabilize one oxidation state than the other.[31] Upon application of ΔT, an uneven concentration distribution of redox ions across the thermogalvanic cells will be developed. The resulting concentration gradient contributes directly to the S_e, a contribution that is further amplified by the reversible dissolution/crystallization of $Fe(CN)_6^{4-}$ ions between the cold and hot electrodes. Apart from the substantial enhancement in S_e, the Hybrid-E_7T_{23} system demonstrates improved ion transport, superior anti-freeze properties, and the capability to form a self-powered QTEC, as shown in **Figure 1d**. Therefore, the synergistic interplay between the co-solvents enables the Hybrid-E_7T_{23} to achieve exceptional thermoelectrochemical performance.

Thermoelectrochemical Performance

The Hybrid-E_xT_y-based QTEC operates on the thermogalvanic effect, wherein a temperature difference across the electrolyte drives reversible redox reactions that establish a potential difference between the electrodes. As illustrated in **Figure 2a**, at the hot electrode, $Fe(CN)_6^{4-}$ undergoes oxidation to $Fe(CN)_6^{3-}$, which releases an electron that travels via the external circuit to the cold electrode. There, it facilitates the reduction of $Fe(CN)_6^{3-}$ back to $Fe(CN)_6^{4-}$. Consistent with thermogalvanic behavior, a linear relationship between steady-state voltage and temperature gradient is observed. The pure PAAm hydrogel electrolyte exhibited a S_e of 1.32 mV K^{-1}, in agreement with previously reported values (**Figure S2**).[15, 31, 36] The introduction of EG or TMP solvents significantly influenced the thermopower, with Hybrid-$E_{30}T_0$ and Hybrid-E_0T_{30} achieving S_e values of 2.0 mV K^{-1} and 2.38 mV K^{-1}, respectively (**Figure S3**). With higher organic solvent content, however, only marginal gains in S_e is achieved and detrimental effect on ionic conductivity occurs. Hence, additional increase in co-solvents concentration was not pursued in this study.

View Article Online
DOI: 10.1039/D6SC03942A

The S_e of the hybrid electrolyte system was optimized through rational design of co-solvents composition to effectively modulates the solvation environment of redox ions. We systematically varied the volume ratios of H_2O, EG, and TMP while maintaining constant PAAm matrix content. **Figure 2b** shows that S_e achieved a maximum of 2.52 mV K^{-1} with a solvent ratio of V_{Water}:V_{EG}:V_{TMP}=7:0.7:2.3, *i.e.,* the Hybrid-E_7T_{23} system. The ionic conductivity (σ) of the electrolytes was also significantly influenced by solvent composition. The pristine PAAm hydrogel exhibited σ = 5.48 S m^{-1}, while that in single-solvent systems decreased to 1.86 S m^{-1} (Hybrid- $E_{30}T_0$) and 2.25 S m^{-1} (Hybrid-E_0T_{30}), as shown in **Figure S4**. However, the rationally designed co-solvents system Hybrid-E_7T_{23} restored conductivity to 4.01 S m^{-1}. Our subsequent analysis suggests that single-solvent addition triggers selective precipitation of $Fe(CN)_6^{4-}$ ions, which enhances thermopower but compromises ionic conductivity. In contrast, the co-solvents approach modifies the solvation structure to facilitate ion transport while maintaining high S_e.

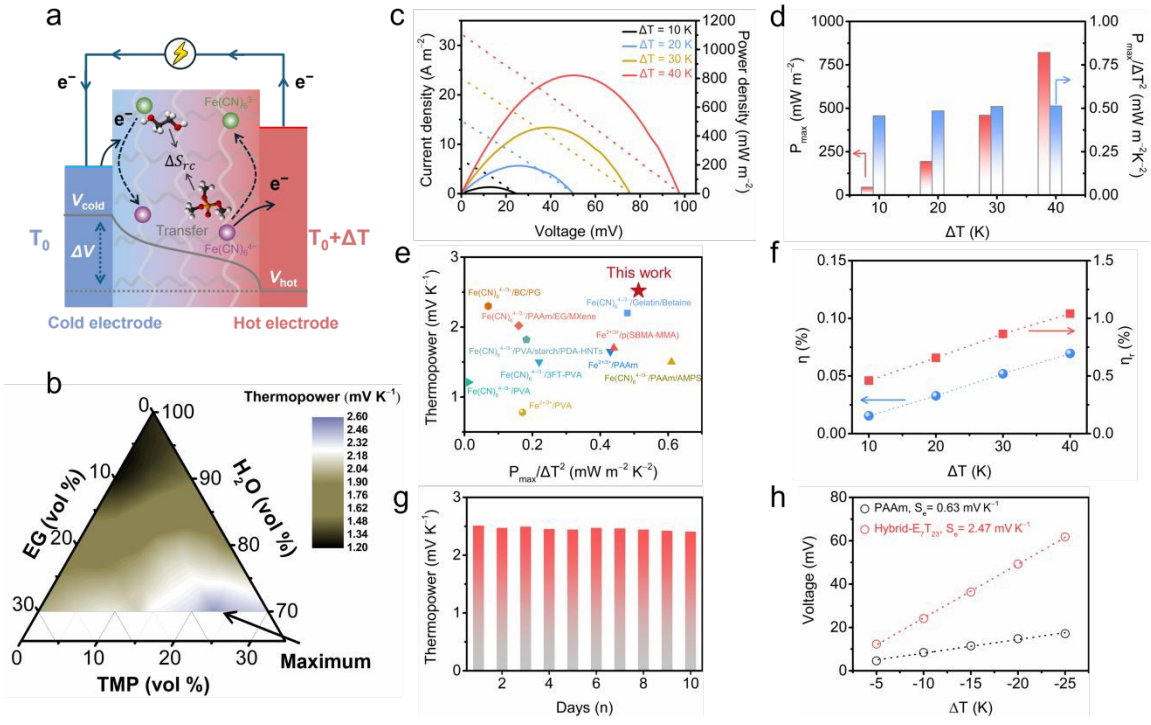

Figure 2. Thermoelectrochemical performance of hybrid electrolytes. (a) Schematic representation of the heat-to-electricity conversion mechanism of QTECs. **(b)** Ternary phase diagram of S_e in Hybrid-E_xT_y with varying volume ratio of EG, TMP, and water. **(c)** Output current−voltage−power curves of

View Article Online
DOI: 10.1039/D6SC03942A

Hybrid-E_7T_{23} at various ΔT, and **(d)** corresponding P_{max} and $P_{max}/\Delta T^2$ values. **(e)** Comparison of S_e versus $P_{max}/\Delta T^2$ for various QTECs. **(f)** Thermal energy conversion efficiency of Hybrid-E_7T_{23}. **(g)** Temporal variation of S_e of Hybrid-E_7T_{23} under a continuous operation of 10 days. **(h)** The S_e of the PAAm electrolyte and Hybrid-E_7T_{23} at sub-zero temperatures.

The thermoelectrochemical performance of the Hybrid-E_7T_{23} was evaluated under varying ΔT. **Figure 2c** depicts the measured output current-voltage-power curves when the cold electrode is maintained at 20 °C. As ΔT increased from 10 K to 40 K, both the open-circuit voltage (V_{oc}) and short-circuit current density (I_{sc}) rise steadily. The corresponding maximum output power (P_{max}) and normalized power density ($P_{max}/\Delta T^2$) are summarized in **Figure 2d**. At $\Delta T = 40$ K, P_{max} reached 821.4 mW m^{-2}, with a normalized power density $P_{max}/\Delta T^2$ of 0.513 mW m^{-2} K^{-2}, in close agreement with theoretical predictions (Note S1, Supporting Information). Notably, this value exceeds those of single-solvent QTECs (0.07 and 0.16) by factors of 7.3 and 3.2, respectively.[29, 31] Further benchmark against previous solvation-modulated QTEC without Gdm-based agents additives confirms significant improvements in both S_e and $P_{max}/\Delta T^2$ (**Figure 2e** and Supplementary Table 2), thus confirming the efficacy of the co-solvents design strategy.

The thermal conductivity (κ) represents another parameter for quantifying heat-to-electricity conversion in QTEC.[37, 38] In contrast to conventional liquid electrolytes, a reduced thermal conductivity of 0.58 W m^{-1} K^{-1} occurs in PAAm hydrogel electrolyte due to restricted convection within its polymer network. The co-solvents strengthen hydrogen-bond networks that restricts molecular collisions and raises viscosity to suppresses internal microconvection.[39] This contributes to further reduction of κ (0.443 W m^{-1} K^{-1}) in the Hybrid-E_7T_{23} electrolyte, a characteristic that favors the maintenance of a stable ΔT across the thermocell (**Figure S5**). The thermoelectrochemical performance of the Hybrid-E_7T_{23} was further assessed by its energy conversion efficiency (η) and Carnot-relative efficiency (η_r). Based on the formulation provided in Note S2 (Supporting Information), the maximum η and η_r respectively reached 0.0695% and 1.04% under a ΔT of 40 K.

View Article Online
DOI: 10.1039/D6SC03942A

Moreover, the Hybrid-E_7T_{23} electrolyte demonstrates excellent moisture retention (**Figure S6**), indicating strong potential for long-term operation. Thus, the assembled QTEC preserves approximately 95.6% of its initial performance, characterized by a high S_e of 2.41 mV K^{-1}, even after ten days (**Figure 2g** and **Figure S7**).

As thermoelectrochemical conversion depends solely on ΔT rather than perceivable heat, we evaluated the electrolyte's heat-to-electricity conversion capability at sub-zero temperatures by fixing the hot electrode at 0 °C. When the cold side was cooled to -25°C, the PAAm electrolyte showed severe performance degradation, yielding a S_e of 0.63 mV K^{-1} due to impeded ion transport and sluggish redox kinetics (**Figure 2h**). In contrast, differential scanning calorimetry (DSC) revealed that the Hybrid-E_7T_{23} electrolyte exhibits a freezing point of -41.8°C, attributable to the co-solvent's disruption of hydrogen-bonding network in water (**Figure S8**). Consequently, the Hybrid-E_7T_{23} electrolyte maintained virtually unaffected thermoelectrochemical performance at sub-zero temperatures. In particular, S_e of 2.47 mV K^{-1} was generated at the same conditions, a value that closely matches the room temperature data to exhibit a superb ~97 % retention (**Figure 2h**). The excellent retention is corroborated by the robust ionic conductivity measured under the low-temperature conditions (**Figure S9**). These results conclusively demonstrate the remarkable anti-freezing properties of our co-solvents QTEC, which allows for sustained thermal energy harvesting at sub-ambient temperatures.

Mechanism of Enhanced Thermoelectrochemical Performance

The enhanced thermoelectrochemical performance of Hybrid-E_7T_{23} can be elucidated via molecular-level interactions. At room temperature, $Fe(CN)_6^{3-}$ remains fully dissolved in hybrid TMP/EG solutions, whereas $Fe(CN)_6^{4-}$ readily precipitates (**Figures S10, S11**). The selective precipitation is also evident in hybrid solutions containing both $Fe(CN)_6^{3-}$ and $Fe(CN)_6^{4-}$ ions, as shown in **Figure S12**. UV-Vis spectra and optical photographs confirm that $Fe(CN)_6^{4-}$ exhibits negligible intrinsic solubility in pure EG solvent (**Figure S13**). X-ray diffraction (XRD) analysis identified the precipitate formed in both pure EG

View Article Online
DOI: 10.1039/D6SC03942A

solvent (**Figure S14**) and hybrid TMP/EG solutions (**Figure S15**) as primarily $Fe(CN)_6^{4-}$, with the characteristic peaks matching the standard Powder Diffraction File of $K_4Fe(CN)_6$. This difference in solubility, as documented in various solvent systems,[31, 40] arises from differential ion-solvent interactions between redox ions that mediate long-range ionic correlations. Furthermore, $Fe(CN)_6^{4-}$ exhibits pronounced thermosensitive solubility as shown in **Figure S16**, which leads to spatial crystallization/dissolution under a temperature gradient. The total S_e in Hybrid-E_xT_y is thus governed by both the solvation entropy difference and the concentration gradient established by the redox couple (**Note S3**).

To validate the formation of a concentration gradient within THs, we characterize the morphologies of the hydrogels using scanning electron microscopy (SEM). As shown in **Figure 3a** and **Figure S17**, the pure PAAm hydrogel exhibits a porous 3D network structure, whereas the surface of Hybrid-E_7T_{23} is covered with abundant micrometer-sized crystals, likely resulting from the precipitation of $Fe(CN)_6^{4-}$ ions. This observation was further corroborated by Raman spectroscopy (**Figure S18**). The crystallization is confined within the hydrogel network, which enables the establishment of a stable concentration gradient across Hybrid-E_7T_{23}. Furthermore, time-of-flight secondary ion mass spectrometry (TOF-SIMS) in positive ion mode revealed a complementary spatial distribution of CH_2N^+ (representing PAAm chains) and K_2FeCN^+ (derived from $K_3Fe(CN)_6$/$K_4Fe(CN)_6$) in Hybrid-E_7T_{23} (**Figure 3b**). The results indicate that the redox ions not only bind to the polymer matrix but also form crystalline phases within the hydrogel. Depth profiling (**Figure S20**) was also applied to probe the distribution of components both on the surface and throughout the bulk of the hydrogel. The uniform distribution, as demonstrated from the resulting 3D reconstruction in **Figure 3c**, ensures coherent ion transport pathways within the electrolyte.

View Article Online
DOI: 10.1039/D6SC03942A

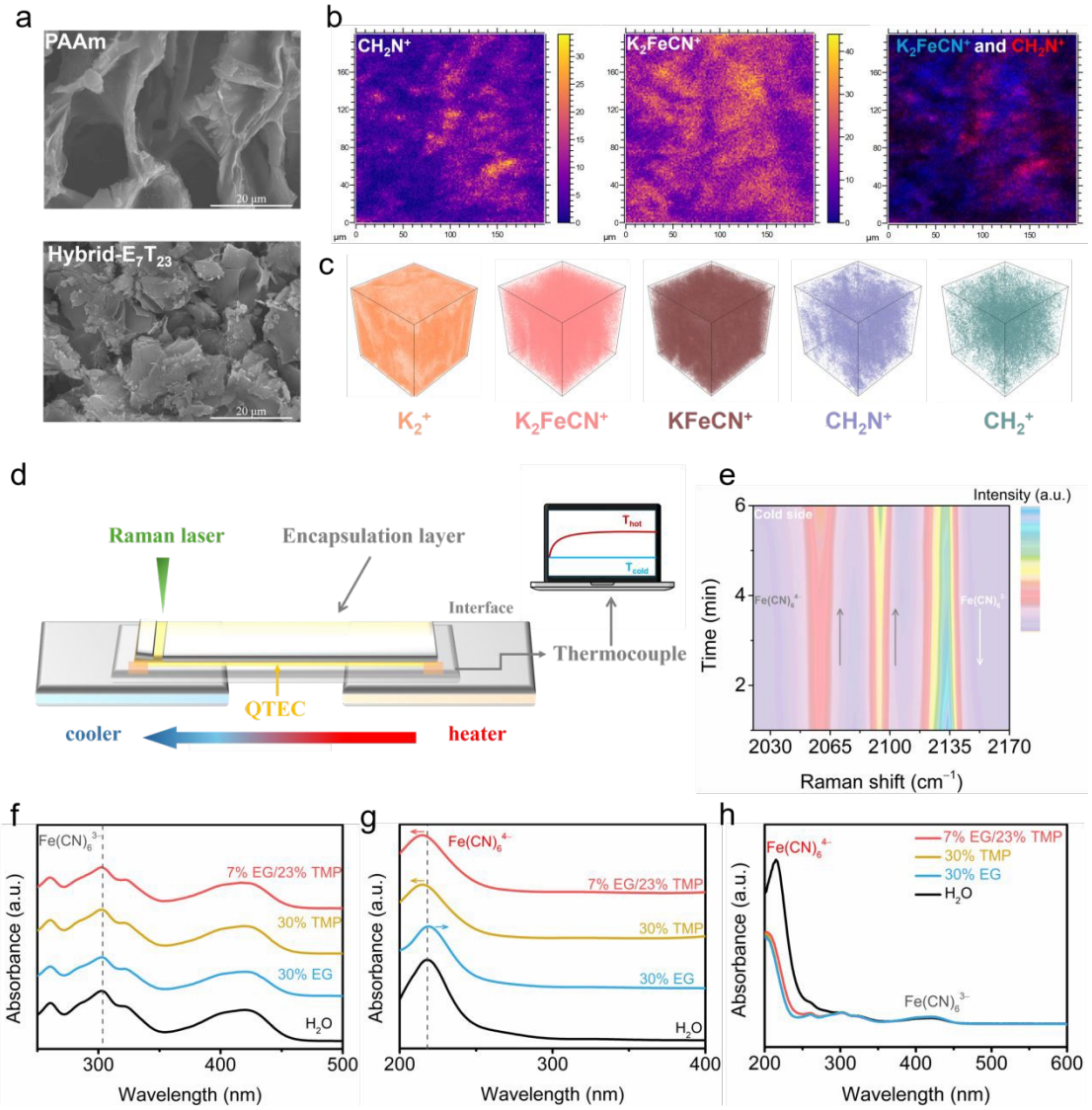

Figure 3. Characterizations of electrolyte structures. (a) Morphological characterization of PAAm electrolyte and Hybrid-E_7T_{23} electrolyte. **(b)** TOF-SIMS 2D spectra and **(c)** 3D reconstruction visual images of several secondary ion fragments in Hybrid-E_7T_{23}. **(d)** Schematic diagram of in-situ Raman measurement setup. **(e)** Real-time monitoring of $Fe(CN)_6^{4-/3-}$ redox couple via in-situ Raman for the cold side of Hybrid-E_7T_{23} at ΔT = 10 K. UV-vis spectra of **(f)** $Fe(CN)_6^{3-}$, **(g)** $Fe(CN)_6^{4-}$, and **(h)** $Fe(CN)_6^{4-/3-}$ aqueous solutions with varying EG/TMP ratios.

During the operation of QTEC, the evolution of local ion concentrations under a ΔT was further examined using in-situ Raman spectroscopy (**Figure 3d**). Characteristic peaks at 2058 and 2093 cm^{-1} can be assigned to $Fe(CN)_6^{4-}$, while a peak at 2132 cm^{-1}

View Article Online
DOI: 10.1039/D6SC03942A

corresponds to $Fe(CN)_6^{3-}$.[39, 41] In the PAAm electrolyte, the $Fe(CN)_6^{3-}$ peak intensity on the cold side decreased with prolonged heating, whereas the $Fe(CN)_6^{4-}$ signal increased (**Figure S21**), which is indicative of ΔT-driven ion transport and redox cycling at the electrodes. In contrast, Hybrid-E_7T_{23} exhibited similar but more pronounced concentration fluctuations under ΔT, with different rates of spectral change (**Figure 3e**). This behavior results from the thermosensitive solubility of $Fe(CN)_6^{4-}$, where reversible crystallization/dissolution under ΔT sustains a stable concentration gradient that leads to additional entropy change of redox reaction for thermopower enhancement.

To determine the relative contributions of solvation entropy differences versus concentration gradients to thermoelectrochemical performance, ultraviolet-visible (UV-vis) spectroscopy was first employed to probe the ion-solvent interactions. **Figure 3f** shows that as the EG/TMP ratio varied, the characteristic absorption peaks of $Fe(CN)_6^{3-}$ remained unchanged in the UV-vis spectra. In contrast, the absorption peak of $Fe(CN)_6^{4-}$ exhibited a noticeable shift from ~218 nm as shown in **Figure 3g**, indicating a stronger interaction between EG/TMP molecules and $Fe(CN)_6^{4-}$ compared to $Fe(CN)_6^{3-}$.[10, 42, 43] These differential ion-solvent interactions not only reduce the solubility of $Fe(CN)_6^{4-}$ but are also believed to enlarge the difference of redox ions' solvation structure.[21, 31, 44] Furthermore, the comparative UV-vis analysis in **Figure 3h** revealed that $Fe(CN)_6^{4-}$ concentration in three Hybrid-E_xT_y electrolytes differs significantly from aqueous electrolytes, while $Fe(CN)_6^{3-}$ concentration remains largely unchanged. This signature correlates strongly with the observed thermosensitive solubility of $Fe(CN)_6^{4-}$ ions in solutions containing solvent molecules. The enhanced S_e in hybrid electrolytes, particularly Hybrid-$E_{30}T_0$ and Hybrid-E_0T_{30}, relative to pure hydrogel electrolytes can be attributed to concentration gradients. However, the similar concentration differences of $Fe(CN)_6^{4-/3-}$ ions are observed across various Hybrid-E_xT_y electrolytes. To isolate solvation entropy contribution, control hydrogel electrolytes designated as Hybrid-E_xT_y (sol) were prepared from the supernatant of equilibrated hybrid solutions. The S_e of Hybrid-E_7T_{23} (sol) reaches 1.67 mV K^{-1}, far

View Article Online
DOI: 10.1039/D6SC03942A

exceeding those of the single solvent electrolytes (**Figure S20**). Therefore, the superior S_e in Hybrid-E_7T_{23} relative to Hybrid-$E_{30}T_0$ and Hybrid-E_0T_{30} originates primarily from ion solvation entropy differences rather than concentration gradient effects.

The above analysis demonstrates that the co-solvents strategy achieves synergistic enhancement through two mechanisms: 1) concentration gradients that enhance performance relative to pure hydrogel; 2) solvation entropy differences that provide the improvement in Hybrid-E_7T_{23} relative to single-solvent hydrogels. Next, spectroscopic analyses were performed to investigate the role of solvent on modulating solvation structures in hybrid electrolytes. Raman spectra of the electrolytes show that the P-O-C vibrational modes in pure TMP, located at 737.6 and 752.8 cm^{-1}, shift noticeably in hybrid electrolytes (**Figure 4a**). This is a consequence of interactions between TMP and other molecules or ions.[45-47] FTIR spectra further confirm these interactions (**Figure 4b**), with characteristic TMP peaks shifting significantly upon hybrid electrolyte formation. Furthermore, TMP addition caused a shift in the O-H vibrational peak, an effect that is amplified by EG (**Figure S23**). These co-solvents-water interactions disrupt the hydrogen-bond network, which is consistent with the observed freezing point depression.[48, 49] The restructured hydrogen-bond network in Hybrid-E_xT_y is further supported by FTIR as shown in **Figure 4c**. A blueshift in the C=O vibration (1600–1700 cm^{-1}) is also observed,[50] likely due to modified polymer-ion coordination and solvation structures. These findings collectively indicate that co-solvents significantly alter the microscopic solvation structure in Hybrid-E_7T_{23}.

Molecular dynamics simulations were performed to elucidate the impact of ion solvation structure on solvation entropy difference. We quantified the composition of solvation structure of redox ions via the number of coordinated oxygen atoms from different species in the Hybrid-E_xT_y. **Figure 4d** shows that more solvents molecules are in the solvation shell of $Fe(CN)_6^{3-}$ than $Fe(CN)_6^{4-}$, consistent with the stronger hydration of higher-valence ions. Owing to its higher dipole moment and Gutmann donor number

View Article Online
DOI: 10.1039/D6SC03942A

relative to the EG,[51] TMP exhibits stronger ion-solvent interactions toward $Fe(CN)_6^{4-}$ ions. The introduction of co-solvents reduces solvent coordination numbers relative to their single-solvent counterparts and the magnitudes of reduction are more significant for EG solvents. Moreover, the number of oxygen atoms from the PAAm backbone coordinating to redox ions shows opposite trends for $Fe(CN)_6^{4-}$ and $Fe(CN)_6^{3-}$ in Hybrid-E_xT_y as compared to single-solvent electrolytes. The result indicates a synergistic co-solvents effect between EG and TMP that facilitates differential binding of PAAm sites to $Fe(CN)_6^{4-/3-}$ ions, a key factor in amplifying the solvation entropy difference. Unlike conventional solvation-engineering strategies that rely solely on bulk liquid-phase regulation,[10, 12] our system demonstrates the active contribution of the polymer matrix.

To obtain deeper molecular insights into the solvation environment, the distribution of oxygen atoms from EG, TMP, and polymer side chains of Hybrid-E_xT_y was examined in **Figure 4e**. The probability distributions of oxygen from the three species, particularly from side chains, around $Fe(CN)_6^{3-}$ are consistently smoother and broader than $Fe(CN)_6^{4-}$. This corresponds to a more disordered and structurally complex solvation shell with greater structural variability of low valence ions. Typical snapshots of solvation shell structures of $Fe(CN)_6^{4-/3-}$ are depicted in **Figure 4f**. Together with the oxygen coordination data, these observations highlight differential solvation structures between the redox ions that directly enhance the solvation entropy difference. Furthermore, ionic conductivity measurements reveal that Hybrid-E_7T_{23} exhibits superior ion transport compared to single-solvent systems. To understand this improvement, we quantified the cation-anion pairing in the electrolyte (**Figure S27**). The results point to a lower degree of K^+ pairing to $Fe(CN)_6^{4-/3-}$ in the co-solvents system, a trend that correlates with the observed increase in ionic conductivity. The co-solvents thus also promote salt dissociation for both $K_3Fe(CN)_6$ and $K_4Fe(CN)_6$, which leads to higher population of free ions available for enhanced ionic conductivity.

View Article Online
DOI: 10.1039/D6SC03942A

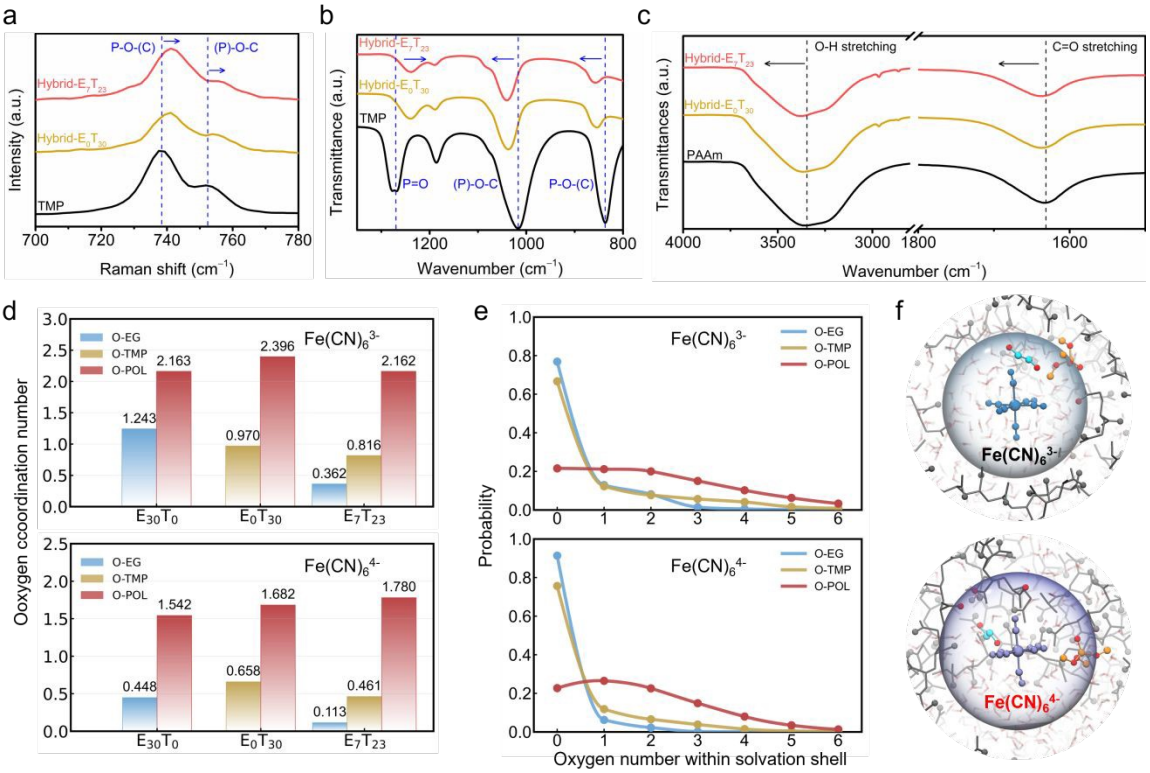

Figure 4. Effect of co-solvents on solvation of redox ions. (a) Raman spectra of various samples. **(b)** FTIR spectra of TMP solvent and various samples. **(c)** FTIR spectra of PAAm electrolyte and various samples. **(d)** Oxygen coordination number of $Fe(CN)_6^{4-/3-}$ ions from EG, TMP, and polymer side chains (POL). **(e)** Probability distribution of oxygen coordination numbers from EG, TMP and POL around $Fe(CN)_6^{4-/3-}$ ions. **(f)** Representative snapshots of the solvation shell structures of $Fe(CN)_6^{3-}$ and $Fe(CN)_6^{4-}$ ions in Hybrid-E_7T_{23} system. Color scheme: $Fe(CN)_6^{4-/3-}$ (blue), solvation shell (large transparent sphere), EG molecules (yellow), TMP molecules (orange), polymer chains (gray). Oxygen atoms (from the three species) within the solvation shells are shown in red spheres. Hydrogen atoms from the three species are omitted for clarity. Water molecules are shown as transparent bonds.

QTEC Durability and Device Application

The QTEC operates continuously, as redox reactions proceed in opposite directions at the hot and cold electrodes while ionic transport replenishes reactants.[52] To evaluate its operational stability, the lifespan of a Hybrid-E_7T_{23} -based QTEC was tested in a quasi-continuous discharge mode at room temperature with ΔT = 10 K. **Figure 5a** shows the voltage over the first 11 cycles. Upon applying the temperature difference, the voltage rises and stabilizes at approximately 25 mV. The QTEC exhibits reproducible cycles of rapid

View Article Online
DOI: 10.1039/D6SC03942A

discharge and recovery during the quasi-continuous discharge mode. The output performance in the 11th cycle (**Figure S28**) shows a maximum power density of 40.2 mW m^{-2}, close to the initial value of 45.5 mW m^{-2}. To enable extended cycling, the thermocell was rested at room temperature (ΔT = 0 K) after every 11 charge-discharge cycles to allow recovery to its initial state. The excellent longevity was demonstrated by a stable thermovoltage of ~24.1 mV even after 110 cycles (**Figure 5b**). During this process, a minor voltage drop is also observed every 11 cycles due to polarization effects. The spontaneous voltage recovery arises from rapid redox ion diffusion that restores local concentration gradients at the electrode interfaces during the open circuit intervals. Furthermore, the Hybrid-E_7T_{23} maintains a stable voltage of ~49.8 mV under a higher ΔT of 20 K as shown in **Figure 5c**, demonstrating its potential for sustained heat-to-electricity conversion under a wide range of ΔT. Under a 2000 Ω load, the thermovoltage peaked and then decayed gradually, while the current density initially rose and then dropped (**Figure S29a**). After 2 hours, the device still delivered ~16.9 mV and ~1.03 A m^{-2}, yielding an energy density of 234 J m^{-2} (**Figure S29b**).

As a harvester of low-grade waste heat, a single QTEC module typically generates insufficient output voltage for practical applications due to the small temperature gradients involved. Device integration is often needed to meet application requirements. We connected 20 individual Hybrid-E_7T_{23}-based QTEC units in series to construct an energy-harvesting device capable of generating useful voltages. As illustrated in **Figure 5d and Figure S30**, the device was fabricated by segmenting the Hybrid-E_7T_{23} hydrogel electrolyte, using graphite plates as electrodes, and connecting the units with copper tape. The assembly was encapsulated in aluminum plastic film to ensure operational stability by shielding it from external interference. When operated under a moderate ΔT of 30 K, the integrated device generated a high output voltage of ~1.26 V, corresponding to a notable S_e of ~42 mV K^{-1} (**Figure 5e**). This performance demonstrates the device's ability to efficiently convert thermal energy into electricity. To assess its practical utility, the device

View Article Online
DOI: 10.1039/D6SC03942A

was used to power electronic components. A light-emitting diode (LED) array was successfully illuminated under $\Delta T = 30$ K (**Figure 5f**). These results confirm the scalability of the Hybrid-E_7T_{23} electrolyte and its practical potential for harvesting accessible low-grade waste heat in real-world applications.

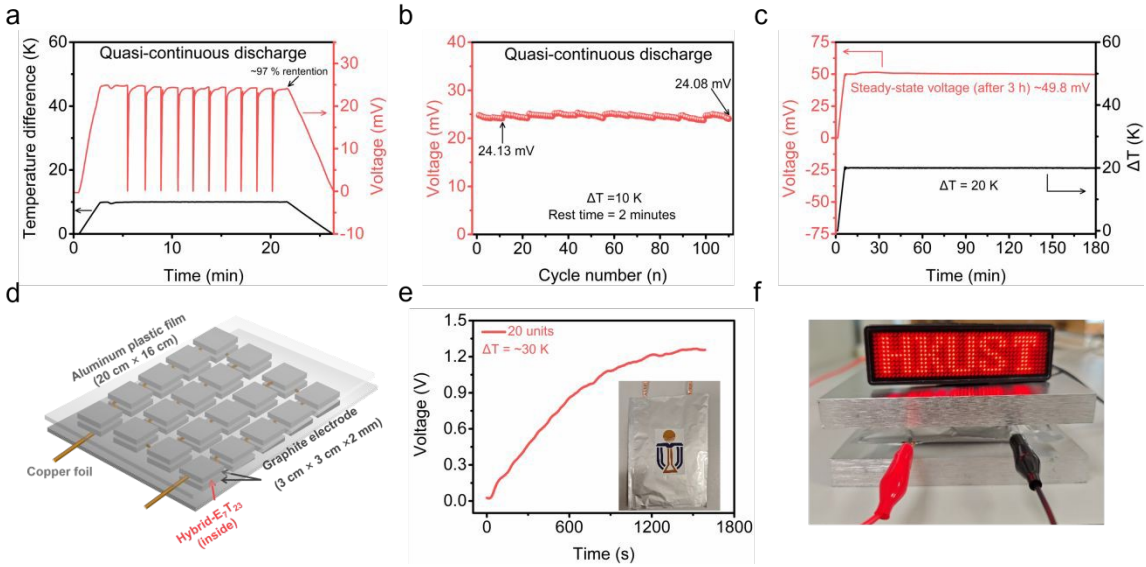

Figure 5. Potential application demonstration. (a) Voltage evolution along with applied temperature difference in the quasi-continuous discharge process for the first 11 cycles. **(b)** Extended voltage life-span for 110 cycles at $\Delta T = 10$ K. **(c)** Stability of the thermal voltage generated by Hybrid-E_7T_{23} for 3 hours. **(d)** Schematic illustration of the integrated module with 20 coupled Hybrid-E_7T_{23}-based QTEC units. **(e)** Voltage–time curve and **(f)** power electronic device for the module at $\Delta T = 30$ K.

III. CONCLUSION

In summary, we developed a co-solvent hydrogel electrolyte for QTECs that exhibit pronounced multiple synergetic effect for low-grade heat harvesting. The co-solvents hydrogel, composed of EG and TMP, leverages robust solvation ability to engineer intrinsic asymmetric solvation environment for $Fe(CN)_6^{4-/3-}$ redox couple. This environment simultaneously enhances the solvation entropy difference and amplifies the concentration gradient of redox ions. The co-solvents-induced restructuring of PAAm coordination sites also promotes differential binding of $Fe(CN)_6^{4-/3-}$ ions. In addition, the co-solvents facilitate salt dissociation that favors continuum ion transport through the

View Article Online
DOI: 10.1039/D6SC03942A

hydrogel. Beyond improving thermoelectrochemical properties, the reconfigured hydrogen-bond network endows the Hybrid-E_7T_{23} electrolyte with anti-freezing capability and long-term stability. As a result, the Hybrid-E_7T_{23} delivers exceptional performance metrics: a S_e increased from 1.32 to 2.52 mV K^{-1}, a normalized power density ($P_{max}/\Delta T^2$) of 0.513 mW m^{-2} K^{-2}, and sustained operation down to sub-zero conditions.

This study demonstrates that co-solvent interactions provide a viable strategy for tuning the solvation environment of redox ions in thermogalvanic hydrogels. The Hybrid-E_7T_{23} system exemplifies this strategy, wherein maximizing the asymmetry between solvation structures resolves the trade-off between thermopower and ionic conductivity. Importantly, the performance enhancement is achieved through a simple, additive-free formulation. Our work presents fresh evidence for the principle that macroscopic properties can be engineered via molecular-level solvation control, thereby reinforcing its potential for the rational design of diverse high-performance, ion-conducting materials.

Acknowledgments

This work is supported by Guangzhou Basic and Applied Basic Research Scheme (No. 2025A04J3996) and Guangzhou-HKUST(GZ) Joint Funding Scheme (No. 2025A03J3872). Computations were performed at the HPC-AI platform of HKUST(GZ). Material characterizations were performed at MCPF and BEST Lab of HKUST-GZ.

View Article Online
DOI: 10.1039/D6SC03942A

REFERENCES

1. Shi, X.-L.; Zou, J.; Chen, Z.-G., Advanced thermoelectric design: From materials and structures to devices, *Chem. Rev.* **2020,** *120* (15), 7399-7515.

2. Liu, Z.; Sato, N.; Gao, W.; Yubuta, K.; Kawamoto, N.; Mitome, M.; Kurashima, K.; Owada, Y.; Nagase, K.; Lee, C.-H.; Yi, J.; Tsuchiya, K.; Mori, T., Demonstration of ultrahigh thermoelectric efficiency of ~7.3% in Mg_3Sb_2/MgAgSb module for low-temperature energy harvesting, *Joule* **2021,** *5* (5), 1196-1208.

3. Zhang, L.; Shi, X.-L.; Yang, Y.-L.; Chen, Z.-G., Flexible thermoelectric materials and devices: From materials to applications, *Mater. Today* **2021,** *46*, 62-108.

4. Lheritier, P.; Torelló, A.; Usui, T.; Nouchokgwe, Y.; Aravindhan, A.; Li, J.; Prah, U.; Kovacova, V.; Bouton, O.; Hirose, S.; Defay, E., Large harvested energy with non-linear pyroelectric modules, *Nature* **2022,** *609* (7928), 718-721.

5. Yu, B.; Duan, J., Electrochemical waste-heat harvesting, *Science* **2023,** *381* (6655), 269-270.

6. Garofalo, E.; Bevione, M.; Cecchini, L.; Mattiussi, F.; Chiolerio, A., Waste heat to power: Technologies, current applications, and future potential, *Energy Technol.* **2020,** *8* (11), 2000413.

7. Liu, C.; Si, Y.; Zhang, H.; Wu, C.; Deng, S.; Dong, Y.; Li, Y.; Zhuo, M.; Fan, N.; Xu, B.; Lu, P.; Zhang, L.; Lin, X.; Liu, X.; Yang, J.; Luo, Z.; Das, S.; Bellaiche, L.; Chen, Y.; Chen, Z., Low voltage–driven high-performance thermal switching in antiferroelectric $PbZrO_3$ thin films, *Science* **2023,** *382* (6676), 1265-1269.

8. Quickenden, T. I.; Mua, Y., A review of power generation in aqueous thermogalvanic cells, *J. Electrochem. Soc.* **1995,** *142* (11), 3985.

9. Abraham, T. J.; MacFarlane, D. R.; Pringle, J. M., High Seebeck coefficient redox ionic liquid electrolytes for thermal energy harvesting, *Energy Environ. Sci.* **2013,** *6* (9), 2639-2645.

10. Duan, J.; Feng, G.; Yu, B.; Li, J.; Chen, M.; Yang, P.; Feng, J.; Liu, K.; Zhou, J., Aqueous thermogalvanic cells with a high Seebeck coefficient for low-grade heat harvest, *Nat. Commun.* **2018,** *9* (1), 5146.

11. Duan, J.; Yu, B.; Huang, L.; Hu, B.; Xu, M.; Feng, G.; Zhou, J., Liquid-state thermocells: Opportunities and challenges for low-grade heat harvesting, *Joule* **2021,** *5* (4), 768-779.

12. Inoue, H.; Zhou, H.; Ando, H.; Nakagawa, S.; Yamada, T., Exploring the local solvation structure of redox molecules in a mixed solvent for increasing the Seebeck coefficient of thermocells, *Chem. Sci.* **2024,** *15* (1), 146-153.

View Article Online
DOI: 10.1039/D6SC03942A

13. Cai, X.; Zeng, Y.; Liu, P.; Zhang, Y.; Wang, L.; Ke, H.; Long, X.; Jiang, H.; Yang, W.; Gan, Z.; Chen, S.; Duan, J., Bioinspired ionic thermoreceptors with anisotropic architecture for thermotactile perception in robots, *Sci. Adv.* **2026,** *12* (21), eaed5473.
14. Meng, H.; Gao, W.; Chen, Y., An ultrathin ionic thermoelectric cell design utilizing near body heat for self-powered wearable electronics, *Nat. Commun.* **2026,** *17* (1), 4684.
15. Zhang, D.; Zhou, Y.; Mao, Y.; Li, Q.; Liu, L.; Bai, P.; Ma, R., Highly antifreezing thermogalvanic hydrogels for human heat harvesting in ultralow temperature environments, *Nano Lett.* **2023,** *23* (23), 11272-11279.
16. Li, Z.; Xu, Y.; Zhang, X., Progresses and insights of thermoelectrochemical devices for low-grade heat harvesting: From mechanisms, materials to devices, *EnergyChem* **2024,** *6* (5), 100136.
17. Lin, W.; Wu, S.; Niu, S.; Hu, Z.; Chen, G.; Liu, Z.; Huang, Y.; Fang, C., Critical design strategy of thermogalvanic hydrogels for low-grade heat harvesting, *Adv. Sci.* **2025,** *12* (31), e06038.
18. Lin, Z.; Hong, J.; Huang, C.; Zhang, X.; Shen, S.; Du, Z.; Zhou, P.; Miao, Y.-B.; Lin, Z.-H.; Lyu, X.; Zou, Z., A strong, tough, and high-efficiency hydrogel thermocell for thermal energy harvesting, *Nano Energy* **2025,** *138*, 110878.
19. Shin, G.; Baek, J. Y.; Kim, J. H.; Lee, J. H.; Kim, H. J.; So, B. J.; Choi, Y.; Yun, S.; Kim, T.; Jeon, J. G.; Kang, T. J., Mechanically adaptable high-performance p(SBMA-MMA) copolymer hydrogel with iron (II/III) perchlorate for wearable thermocell applications, *Adv. Funct. Mater.* **2025,** *35* (12), 2412524.
20. Chen, Y.; Huang, Q.; Liu, T.-H.; Qian, X.; Yang, R., Effect of solvation shell structure on thermopower of liquid redox pairs, *EcoMat* **2023,** *5* (9), e12385.
21. Li, S.; Li, Z.; Xu, D.; Hu, R., Strong concentration gradient effect and weak solvation effect in thermopower enhancement in $K_3Fe(CN)_6$/ $K_4Fe(CN)_6$ aqueous electrolyte with ethanol addition, *Chem. Eng. J.* **2024,** *493*, 152806.
22. Zeng, Y.; Yu, B.; Chen, M.; Zhang, J.; Liu, P.; Guo, J.; Wang, J.; Feng, G.; Zhou, J.; Duan, J., Solvation entropy engineering of thermogalvanic electrolytes for efficient electrochemical refrigeration, *Joule* **2025,** *9* (3).
23. Liu, Y.; Zhang, S.; Zhou, Y.; Buckingham, M. A.; Aldous, L.; Sherrell, P. C.; Wallace, G. G.; Ryder, G.; Faisal, S.; Officer, D. L.; Beirne, S.; Chen, J., Advanced wearable thermocells for body heat harvesting, *Adv. Energy Mater.* **2020,** *10* (48), 2002539.
24. Xu, C.; Sun, Y.; Zhang, J.; Xu, W.; Tian, H., Adaptable and wearable thermocell based on stretchable hydrogel for body heat harvesting, *Adv. Energy Mater.* **2022,** *12* (42), 2201542.
25. Zhang, D.; Mao, Y.; Ye, F.; Li, Q.; Bai, P.; He, W.; Ma, R., Stretchable thermogalvanic

View Article Online
DOI: 10.1039/D6SC03942A

hydrogel thermocell with record-high specific output power density enabled by ion-induced crystallization, *Energy Environ. Sci.* **2022,** *15* (7), 2974-2982.

26. Lu, X.; Xie, D.; Zhu, K.; Wei, S.; Mo, Z.; Du, C.; Liang, L.; Chen, G.; Liu, Z., Swift assembly of adaptive thermocell arrays for device-level healable and energy-autonomous motion sensors, *Nano Micro Lett.* **2023,** *15* (1), 196.

27. Gui, J.-X.; Cheng, Y.; Ren, K.; Liu, Z.-P.; Zhu, Z.; Xue, Z.-Y.; Zhu, Y.; Wang, R.-H.; Pei, G.; Sui, J.; Chen, L.-F., Development of ternary hydrogel electrolytes for superior gel thermocells: Exceptional anti-drying, anti-freezing, and mechanical robustness, *Adv. Mater.* **2025,** *37* (14), 2420214.

28. Yu, B.; Duan, J.; Cong, H.; Xie, W.; Liu, R.; Zhuang, X.; Wang, H.; Qi, B.; Xu, M.; Wang, Z. L.; Zhou, J., Thermosensitive crystallization–boosted liquid thermocells for low-grade heat harvesting, *Science* **2020,** *370* (6514), 342-346.

29. Li, J.; Chen, S.; Han, Z.; Qu, X.; Jin, M.; Deng, L.; Liang, Q.; Jia, Y.; Wang, H., High performance bacterial cellulose organogel-based thermoelectrochemical cells by organic solvent-driven crystallization for body heat harvest and self-powered wearable strain sensors, *Adv. Funct. Mater.* **2023,** *33* (46), 2306509.

30. Liu, L.; Zhang, D.; Bai, P.; Mao, Y.; Li, Q.; Guo, J.; Fang, Y.; Ma, R., Strong tough thermogalvanic hydrogel thermocell with extraordinarily high thermoelectric performance, *Adv. Mater.* **2023,** *35* (32), 2300696.

31. Liu, Z.; Hu, Y.; Lu, X.; Mo, Z.; Chen, G.; Liu, Z., Electrolyte engineering of quasi-solid-state thermocells for low-grade heat harvest at sub-zero temperatures, *Adv. Energy Mater.* **2024,** *14* (42), 2402226.

32. Dupont, M. F.; MacFarlane, D. R.; Pringle, J. M., Thermo-electrochemical cells for waste heat harvesting–progress and perspectives, *Chem. Commun.* **2017,** *53* (47), 6288-6302.

33. Xu, Y.; Li, Z.; Li, S.; Zhang, S.; Zhang, X., Reversibly tuning thermopower enabled by phase-change electrolytes for low-grade heat harvesting, *Energy Environ. Sci.* **2025,** *18* (2), 750-761.

34. Yu, H.; Liu, X.; Li, M.; Zhang, H.; Wang, Y.; Zhu, M.; Luo, S.; Zhang, X.; Liu, Z.; Yang, Y.; Chen, W.; Hu, Z.; Wang, K.; Meng, W.; Huang, Z.; Liu, Z.; Huang, Y., Constructing High-Power N-Type Thermocells via Fluoride-Mediated Imidazole–Iodine Coordination, *Angew. Chem.* **2026,** *138* (15), e25056.

35. Gao, W.; Lei, Z.; Zhang, C.; Liu, X.; Chen, Y., Stretchable and freeze-tolerant organohydrogel thermocells with enhanced thermoelectric performance continually working at subzero temperatures, *Adv. Funct. Mater.* **2021,** *31* (43), 2104071.

36. Shi, X.; Ma, L.; Li, Y.; Shi, Z.; Wei, Q.; Ma, G.; Zhang, W.; Guo, Y.; Wu, P.; Hu, Z.,

View Article Online
DOI: 10.1039/D6SC03942A

Double hydrogen-bonding reinforced high-performance supramolecular hydrogel thermocell for self-powered sensing remote-controlled by light, *Adv. Funct. Mater.* **2023,** *33* (9), 2211720.

37. Liu, Y.; Cui, M.; Ling, W.; Cheng, L.; Lei, H.; Li, W.; Huang, Y., Thermo-electrochemical cells for heat to electricity conversion: from mechanisms, materials, strategies to applications, *Energy Environ. Sci.* **2022,** *15* (9), 3670-3687.

38. Yu, M.; Li, H.; Li, Y.; Wang, S.; Li, Q.; Wang, Y.; Li, B.; Zhu, K.; Liu, W., Ionic thermoelectric gels and devices: Progress, opportunities, and challenges, *EnergyChem* **2024,** *6* (3), 100123.

39. Lu, X.; Mo, Z.; Liu, Z.; Hu, Y.; Du, C.; Liang, L.; Liu, Z.; Chen, G., Robust, efficient, and recoverable thermocells with zwitterion-boosted hydrogel electrolytes for energy-autonomous and wearable sensing, *Angew. Chem. Int. Ed.* **2024,** *63* (29), e202405357.

40. Tanaka, Y.; Wake, A.; Inoue, D.; Moritomo, Y., Concentration gradient effect in liquid thermoelectric device composed of organic-solvent-added aqueous solution containing $K_4[Fe(CN)_6]/K_3[Fe(CN)_6]$, *Jpn. J. Appl. Phys.* **2024,** *63* (1), 014002.

41. Wang, Y.; Zhang, Y.; Xin, X.; Yang, J.; Wang, M.; Wang, R.; Guo, P.; Huang, W.; Sobrido, A. J.; Wei, B.; Li, X., In situ photocatalytically enhanced thermogalvanic cells for electricity and hydrogen production, *Science* **2023,** *381* (6655), 291-296.

42. Liu, Y.; Yin, L.; Chen, S.; Liu, Y.; Liu, Q.; Yang, L.; Li, Y.; Zhang, Q.; Huang, Y., A hydrogel thermoelectrochemical cell with high self-healability and enhanced thermopower both induced by zwitterions, *J. Mater. Chem. A* **2024,** *12* (29), 18582-18592.

43. Liu, L.; Zhang, D.; Bai, P.; Fang, Y.; Guo, J.; Li, Q.; Ma, R., Fatigue-resistant and super-tough thermocells, *Nat. Commun.* **2025,** *16* (1), 1963.

44. Wu, H.; Song, J.; Gao, N.; Pang, X.; Li, Y.; Xu, Z.; Yu, X., High performance eutectogel-based thermocell with a wide operating temperature range through a water-containing deep eutectic solvent strategy, *Chem. Eng. J.* **2025,** *505*, 159714.

45. Lin, W.; Chen, D.; Yu, J., Manipulating the ionic conductivity and interfacial compatibility of polymer-in-dual-salt electrolytes enables extended-temperature quasi-solid metal batteries, *J. Colloid Interface Sci.* **2024,** *666*, 189-200.

46. Ni, J.; Cheng, Q.; Wang, M.; Liu, S.; Ji, H.; He, Y.; Qian, T.; Yan, C.; Lu, J., Reshaping hydrogen bond network in aqueous-aprotic hybrid electrolyte to achieve highly selective ambient ammonia synthesis, *Applied Catalysis B: Environment and Energy* **2024,** *351*, 123944.

47. Chen, J.; Lin, W.; Wu, Z.; Chen, D.; Law, H. M.; Ciucci, F.; Yu, J., A coordination-reinforced and encapsulated polymer electrolyte for durable and safe Na-metal batteries, *Energy Storage Mater.* **2026,** *84*, 104834.

View Article Online
DOI: 10.1039/D6SC03942A

48. Dai, B.; Shi, X.; Pei, X.; Xu, F.; Zhao, Y., Synergistic dual co-solvents hybrid electrolyte design enabling high-voltage flexible aqueous lithium-ion fiber batteries, *Energy Storage Mater.* **2024,** *66*, 103231.

49. Lin, L.; Shao, Z.; Liu, S.; Yang, P.; Zhu, K.; Zhuang, W.; Li, C.; Guo, G.; Wang, W.; Hong, G.; Wu, B.; Zhang, Q.; Yao, Y., High-entropy aqueous electrolyte induced formation of water-poor Zn^{2+} solvation structures and gradient solid-electrolyte interphase for long-life Zn-metal anodes, *Angew. Chem. Int. Ed.* **2025,** *64* (15), e202425008.

50. Hu, X.; Feng, L.; Xie, A.; Wei, W.; Wang, S.; Zhang, J.; Dong, W., Synthesis and characterization of a novel hydrogel: salecan/polyacrylamide semi-IPN hydrogel with a desirable pore structure, *J. Mater. Chem. B* **2014,** *2* (23), 3646-3658.

51. Wu, S.; Luo, Y.; Niu, S.; Lin, W.; Fang, C., AI-informed solvation engineering for thermogalvanic electrolytes with high thermopower, *The Journal of Physical Chemistry Letters* **2025,** *16* (46), 12010-12017.

52. Hu, R.; Cola, B. A.; Haram, N.; Barisci, J. N.; Lee, S.; Stoughton, S.; Wallace, G.; Too, C.; Thomas, M.; Gestos, A.; Cruz, M. E. d.; Ferraris, J. P.; Zakhidov, A. A.; Baughman, R. H., Harvesting waste thermal energy using a carbon-nanotube-based thermo-electrochemical cell, *Nano Lett.* **2010,** *10* (3), 838-846.

View Article Online
DOI: 10.1039/D6SC03942A

The data supporting this article have been included as part of the Supplementary Information.